Effect of Vegard strains on the extrinsic size effects in ferroelectric nanoparticles

Anna N. Morozovska,[1,*] Iryna S. Golovina,[2,*] Sergiy V. Lemishko,[2,3] Alexander A. Andriiko,[3]
Sergiy A. Khainakov,[4] and Eugene A. Eliseev[5]

[1]*Institute of Physics, National Academy of Sciences of Ukraine, 46, pr. Nauki, 03028 Kyiv, Ukraine*
[2]*Institute of Semiconductor Physics, National Academy of Sciences of Ukraine, 41, pr. Nauki, 03028 Kyiv, Ukraine*
[3]*National Technical University of Ukraine, "Kyiv Polytechnic Institute," 03056 Kyiv, Ukraine*
[4]*Department of Organic and Inorganic Chemistry, University of Oviedo, 33006 Oviedo, Spain*
[5]*Institute of Problems for Material Sciences, National Academy of Sciences of Ukraine, 3, Krjijanovskogo, 03068 Kyiv, Ukraine*

(Received 7 October 2014; revised manuscript received 14 November 2014; published 5 December 2014)

By changing the size and the shape of ferroelectric nanoparticles, one can govern their polar properties, including their improvement in comparison with the bulk material. The shift of the ferroelectric transition temperature can reach hundreds of degrees Kelvin. A phenomenological description of these effects was proposed in the framework of Landau-Ginsburg-Devonshire (LGD) theory using the concepts of surface tension and surface bond contraction. However, this description contains a series of poorly defined parameters, and the physical nature is ambiguous. It appears that the size and shape dependences of the phase transition temperature, along with all polar properties, are defined by the nature of the size effect. Existing LGD-type models do not take into account that defect concentration strongly increases near the particle surface. In order to develop an adequate phenomenological description of size effects in ferroelectric nanoparticles, one should consider Vegard strains (local lattice deformations) originating from defect accumulation near the surface. In this paper, we propose a theoretical model that takes into account Vegard strains and performs a detailed quantitative comparison of the theoretical results with experimental ones for quasispherical $KTa_{1-x}Nb_xO_3$ nanoparticles (average radius 25 nm), which reveal the essential (about 100 K) increase of the transition temperature in spherical nanoparticles in comparison with bulk crystals. From the comparison between the theory and experiment, we established the leading contribution of Vegard strains to the extrinsic size effects in ferroelectric nanoparticles. We determined the dependence of Vegard strains on the content of Nb and reconstructed the Curie temperature dependence on the content of Nb using this dependence. The dependence of the Curie temperature on the Nb content becomes a nonmonotonic one for the small (<20 nm) elongated $KTa_{1-x}Nb_xO_3$ nanoparticles. We established that the accumulation of intrinsic and extrinsic defects near the surface can play a key role in the physical origin of extrinsic size effects in ferroelectric nanoparticles and govern its main features.

DOI: 10.1103/PhysRevB.90.214103 PACS number(s): 77.84.Ek, 77.80.bn

I. INTRODUCTION

The study of unique physical properties of ferroelectric nanoparticles attracts the attention of researchers. Yadlovker and Berger [1–3] present unexpected experimental results that reveal the enhancement of polar properties of cylindrical nanoparticles of Rochelle salt. The authors of Refs. [4–6] successfully managed the temperature of the ferroelectric phase transition and the magnitude and position of the maximum of the dielectric constant for nanopowders and nanoceramics of barium titanate and lead titanate. The studies of $KTaO_3$ nanopowders [7–10] and nanograined ferroelectrics of $KNbO_3$ and $KTa_{1-x}Nb_xO_3$ [11–13] revealed new polar and magnetic phases and the shift of phase transition temperature in comparison with bulk crystals.

Theoretical consideration of manifold size effects allows one to establish the physical origin of the transition temperature shift and phase diagram changes appearing under the decrease of nanoparticle sizes. In particular, using the continual phenomenological approach, Perriat *et al.* [14], Huang *et al.* [15,16], Morozovska *et al.* [17,18,20], Eliseev *et al.* [21], and Ma [22] have shown that the changes of the transition temperatures and the enhancement or weakening of polar properties are conditioned by different "extrinsic" and "intrinsic" size effects in nanoparticles. The partition is tentative and specified by the size effect manifestation. Size effect classification in ferroelectric nanoparticles is given in the first column of Table I.

As a rule, the term "extrinsic size effects" implies that its consequences depend on the size and the shape of the particle but not on its internal state (e.g., not the gradients of physical properties inside the nanoparticle). The contribution of the extrinsic size effecst leads to the shift of the transition Curie temperature from the paraelectric to ferroelectric phase that is proportional to either $1/R$ [14,17–21] or $1/R^2$ [15], depending on the model, where R is the curvature radius of the nanoparticles surface (e.g., it is the radius of the spherical particle). For instance, if one considers intrinsic surface stress (see, e.g., Ref. [23]) under the curved surface of solid bodies, it leads to isotropic compression of the particles, resulting in the shift of the transition temperature proportional to $Q\mu/R$, where μ is the coefficient of the surface stress (similar to the surface tension coefficient determining the surface energy in liquids). The form of the "effective" electrostriction constant Q essentially depends on the shape of the particle, having different signs for the cylinders and spheres of perovskite ferroelectrics [17–21]. In the "surface bond contraction" model [15], the shift of the Curie temperature is proportional to the ratio χ/R^2, and

*Corresponding author: anna.n.morozovska@gmail.com or isgolovina@ukr.net

TABLE I. Size effects of Curie temperature in ferroelectric nanoparticles.

Contribution to size effect (and its origin)	Size dependence of Curie temperature shift and dependence on the particle radius R		Size effect type	Ref.
	Spherical particle of radius R	Ellipsoid or wire of radius R with polarization directed along the longer axes $L \gg R$		
Surface stress (from the surface tension)	$-\frac{2\mu(2Q_{12}+Q_{11})}{\alpha_T R}$	$-\frac{4\mu Q_{12}}{\alpha_T R}$	Extrinsic ($\sim 1/R$)	[17,18]
	μ is a surface stress (tension) coefficient that is positive, Q_{ij} are electrostriction coefficients, and α_T is the temperature coefficient of dielectric stiffness			
Surface bond contraction (from the surface curvature)	$\frac{4Y}{\alpha_T}\frac{\delta a}{a}\frac{(na)^2}{R^2}$	$\frac{2Y}{\alpha_T}\frac{\delta a}{a}\frac{(na)^2}{R^2}$	Extrinsic ($\sim 1/R^2$)	[15,16]
	Y is the Young modulus, δa is the contraction of a lattice constant a, and n is the number of contracted layers; factor $\chi = \frac{4Y}{\alpha_T}\frac{\delta a}{a}(na)^2$			
Vegard strains/stresses (from defect accumulation)	$\frac{-2\eta(Q_{11}+2Q_{12})}{\alpha_T(s_{11}+2s_{12})}\frac{R_0^2}{R^2}$	$\frac{-4\eta Q_{12}}{\alpha_T(s_{11}+s_{12})}\frac{R_0^2}{R^2}$	Extrinsic ($\sim 1/R^2$)	This work
	η is the Vegard strain, R_0 is the defect layer thickness, and s_{ij} are elastic compliances			
Depolarization, correlation, and spontaneous flexoelectric effects (from electric field and polarization gradients)	$\frac{-(g/\alpha_T)}{(g/n_d)+(\lambda+\sqrt{g/n_d})(R/3)}$ $\lambda > 0$ $n_d = \frac{1}{(\varepsilon_b+2\varepsilon_e)\varepsilon_0}$ is a depolarization factor	$-\frac{2}{\alpha_T}\left(\frac{g}{R\lambda+R^2/4}\right), \quad \lambda > 0,$ $-\frac{2}{\alpha_T}\left(g\frac{2\lambda-R}{2R\lambda^2}\right), \quad \lambda < 0.$ The shift from the depolarization field is negligibly small, and absent in the limit of a wire when $L/R \to \infty$	Intrinsic (R dependence is complex)	[17,18,27]
	λ is the extrapolation length, g is the polarization gradient term, n_d is a depolarization factor, ε_b is the background permittivity of ferroelectrics [28], and ε_e is the permittivity of external media			

the value of the factor χ is determined by the surface bond contraction to the lattice parameter ratio $\delta a/a$ [Table I]. The influence of extrinsic size effects is essential for the particles with a curvature radius (or size) smaller than 50–100 nm.

The known intrinsic size effects of ferroelectric nanoparticles are determined mainly by the long-range gradient of the depolarizing electric field inside the particle and the short-range (or "chemical") polarization gradient near the surface [24]. They lead to the more complicated dependence of the transition temperature on the shape and size of the particles, primarily due to a nontrivial dependence of the electrical depolarization fields and flexoelectric strains on particle shape, the orientation of the ferroelectric polarization, and the conditions of its screening near the particle surface [17–21]. As a rule, the influence of intrinsic size effects is essential for the particles with sizes less than 10 nm; the internal scale of polarization is determined by the correlation length, which is typically less than 0.5 nm in spherical particles due to the depolarization effect; and the deviation from the bulk polarization is governed by the so-called extrapolation length λ that is about 0.5–2 nm [25,26].

Therefore, the analysis of the experimentally observed transition temperature dependence on the particles sizes allows one to establish the nature of size effects in the studied system and to determine corresponding phenomenological parameters like μ, χ, or λ from the fitting of experimental data with the adequate theoretical model. Despite this, it remains to be realized for the majority of nanostructured systems. Probably, the difficulties are mostly due to existing phenomenological considerations of ferroelectric particles not being adequate for real nanoparticles with strongly strained near-surface layers, where the strains or stresses are caused by the accumulation of defects (impurities and vacancies) in the region. Indeed, it is well established that the defects concentration noticeably increases near the particle surface, allowing for the essential lowering of their formation energies [27–29]. The abrupt, spontaneous polarization near the surface of ferroelectrics causes the strong accumulation of ions and charged vacancies in the spatial regions to screen the bond surface charges [30–33]. In turn, vacancies and ion accumulations near the surfaces of solids produce surface stresses [34] that substantially alter thermodynamic equilibrium [35], leading to the changes of phase diagrams and transition temperatures.

In order to develop an adequate thermodynamic description of size effects in ferroelectric nanoparticles, one has to determine the microscopic nature of phenomenological parameters and relate them to the lattice deformation near the particle surface due to the defect accumulation. The analysis of our experimental results has shown that the concept of compositionally induced expansion [34] (or chemical pressure [36]) originated from the Vegard strains [37,38] is consistent with our model. According to this concept, the inclusion of a defect

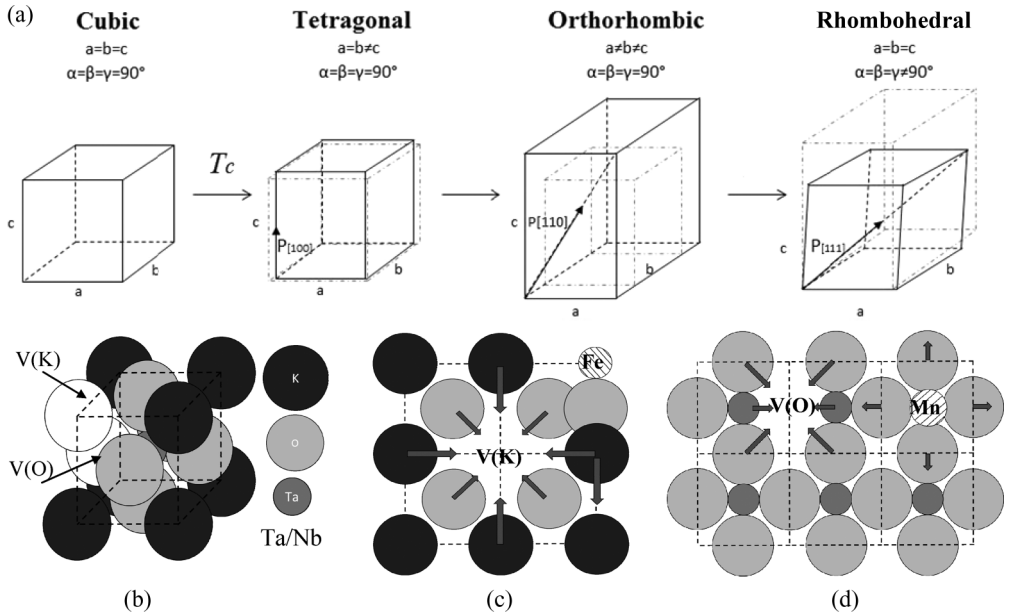

FIG. 1. (a) Sequence of phase and structural transformations in $KTa_{1-x}Nb_xO_3$. (b) Intrinsic defects in $KTa(Nb)O_3$ lattice. (c) and (d) Local lattice deformations caused by intrinsic [oxygen and potassium vacancies, V(O) and V(K)] and extrinsic (Fe^{3+} or Mn^{2+} ions) defects.

(impurity ion or vacancy) leads to the local deformation of the crystal lattice, and the action of many defects causes a strain proportional to their concentration. In this case, the proportionality coefficient is determined either from *ab initio* calculations [38] or from experiments [39,40]. It should be noted that the influence of the Vegard strain, coming from the diffusion and the accumulation of defects near the interfaces of ferroelectric thin films, results in the pronounced change of their polar properties [41,42]. Therefore, it is natural to expect that one could not neglect Vegard strains when describing polar properties of ferroelectric nanoparticles. Also, a steric effect [43,44] takes place for the strong accumulation ("crowding") of defects.

Thus, we performed the modeling of the transition temperatures for ferroelectric nanoparticles taking into account the Vegard strains. Theoretical results are analyzed and compared with the experiment for $KTa_{1-x}Nb_xO_3$ nanoparticles.

II. THEORETICAL MODEL

A. Model background for the $KTaO_3$-$KNbO_3$ system

It was experimentally established that extrinsic and intrinsic defects play a crucial role in the emerging of polar properties in $KTa_{1-x}Nb_xO_3$ nanocrystals [8–10,13]. Thus, due to the presence of the dipole centers associated with Fe^{3+} ions (the centers of axial and rhombic symmetries), ferroelectric phase transition occurs in nanocrystalline $KTaO_3$ at 29 K [7,8], while the bulk material is a quantum paraelectric [45]. These centers include oxygen vacancies in their structure and are formed mainly near the surface of the particles, as the concentration of oxygen vacancies has a sharp maximum in the surface layer.

Note the main features of polar and structural phase transitions in the considered system. Bulk $KTaO_3$ is a quantum paraelectric having a cubic structure down to 0 K [45]. At the same time, $KNbO_3$ and solid solutions of $KTa_{1-x}Nb_xO_3$ ($x > 0.2$) undergo three successive phase transitions, namely, from the cubic paraelectric to tetragonal ferroelectric phase at Curie temperature (T_C) and then two structural transitions, with the polarization vector P, switching between different crystallographic directions [Fig. 1(a)]. Also, as shown in Ref. [46], T_C shifts almost linearly under the changes of the Nb content x in the $KTa_{1-x}Nb_xO_3$ solid solution. Below we consider the dependence of the Curie temperature on the composition under the decreasing size of the crystals for two particle shapes.

In the solid solutions considered, the most prevalent intrinsic defects are vacancies of oxygen and potassium [Fig. 1(b)]. Iron and manganese ions are mostly registered among the extrinsic defects [Figs. 1(c) and 1(d)], which are incorporated into the lattice during the synthesis as unavoidable impurities [9,13]. Figure 1(b) gives an idea of the atomic arrangement and intrinsic defects (oxygen and potassium vacancies) in the $KTa(Nb)O_3$ lattice. Figure 1(c) demonstrates different possibilities of lattice strain appearance in the presence of an impurity Fe^{3+} ion and/or potassium vacancy. In the first case, the Fe^{3+} ion occupies a site of the potassium ion K^+, and an oxygen ion invades as the charge compensator in the nearest intersite, which leads to strong local stretching of the lattice. The local lattice contraction occurs under the potassium vacancy formation. Corresponding atomic displacements are indicated by arrows. Figure 1(d) demonstrates the different possibilities of lattice strain in the presence of an impurity Mn^{2+} ion and/or oxygen vacancy. In the first case, the Mn^{2+} ion occupies the site of the Ta^{5+}/Nb^{5+} ion, and an oxygen vacancy is formed as a charge compensator in the immediate environment. The result is a local extension of the lattice around the impurity ion and its local contraction around oxygen vacancy. Corresponding atomic displacements are indicated by arrows.

It is known that the concentration of defects inside the crystal is inhomogeneous and strongly increases from the bulk to the surface of the particle [34,35]. Since the near-surface

layer is enriched with defects, here the crystal lattice becomes either "spongy" or "denser" depending on the type of defect [Figs. 1(b)–1(d)], meaning that the lattice parameter is also locally changed.

With the presence of different types of defects, resulting in either expansion or compression of the lattice, the surface of the particle may have a complicated relief structure. However, the ensemble of weakly interacting or noninteracting particles most probably can be considered as an effective ensemble of ellipsoids with different aspect ratios of the semiaxes R and L. In our calculations, we change the curvature of the surface $1/R$ and calculate the Curie temperature for two limiting forms of the particle, namely the sphere and very prolate ellipsoid. Thus, R is either the sphere radius or the smaller semiaxis of the ellipsoid hereinafter.

B. Basic equations

1. Core and shell model for Vegard pressure calculations

Possible lattice deformations caused by intrinsic [vacancies $V(\mathrm{O})$ and $V(\mathrm{K})$] and extrinsic (Fe^{3+} or Mn^{2+} ions) defects are shown in Figs. 1(b)–1(d). Following Huang *et al.* [15] and using the concept of compositionally induced expansion or contraction introduced by Sheldon and Shenoy [34], the defect accumulation under a curved surface produces effective stresses of the inner part of the particle. The screening of the depolarization field at the surface and outside of the particle leads to the exponential decrease of charged defect concentration when moving away from the surface [34]. In addition, the characteristic thickness of the layer enriched by defects is determined by the screening length, and their maximal concentration is limited by a steric effect [41,42]. Based on the abovementioned results, we perform an elementary speculation leading to the semipostulated expression for the hydrostatic pressure acting on the inner part of an ellipsoidal particle with semiaxes R and $L(R \leqslant L)$ [Fig. 2].

In accordance with the Vegard law [37], local changes in the concentration of defects lead to the appearance of additional sources for elastic strains $\delta\eta_{ij} = \tilde{W}^d_{ij}\delta N_d$, where W^d_{ij} are the Vegard stress tensor components for defects of the type "d"; $\delta N_d(\vec{r}) = N_d(\vec{r}) - N_{de}$ is the difference between the "instant" concentration of defects $N_d(r)$ in the point $\mathbf{r}$ and their equilibrium (average) concentration N_{de}. Hereinafter, the Vegard tensor is diagonal, i.e., $\tilde{W}^d_{ij} = W\delta_{ij}$ (δ_{ij} is the Kronecker delta symbol). For perovskites ABO_3, the absolute values of W related to vacancies can be estimated as $|W| \propto (10{-}10^2)$ Å^3 [38], and so the corresponding strains $\delta u_{ij}(r)$ can reach percentages for a high variation of defect concentration $\delta N_d \sim 10^{27}\mathrm{m}^{-3}$. Assuming that most defects are located in the ultrathin layer under the particle surface and their concentration decreases exponentially towards the particle bulk [34], we can approximately consider the particle consisting of an ultrathin "shell" of thickness $R_0 \ll R$ highly enriched by defects and the remaining "core" of radius $R - R_0 \approx R$ without them, i.e., $\delta N_d = 0$ in the core and $\delta N_d = N_d$ in the shell. Depending on the Vegard stress sign, the mechanism leads to the tangential compressive or tensile strain $\delta\eta_{11} = \delta\eta_{22} = W\delta N_d$, which exists in the shell of thickness R_0. For the sake of brevity, the strain is further denoted as η, i.e., $\eta \equiv W\delta N_d$. Then, using eqs. (1) and (3)

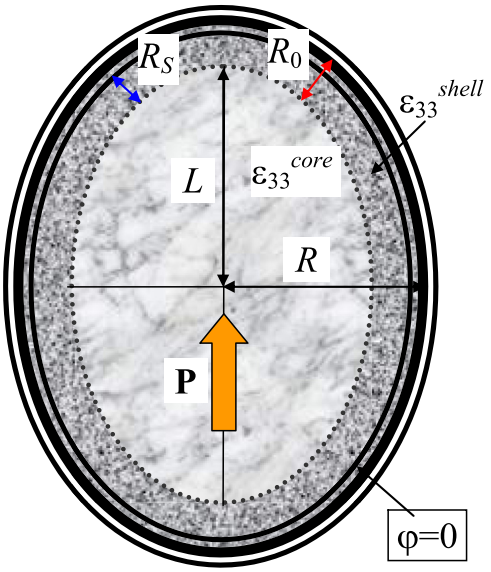

FIG. 2. (Color online) Schematics of an ellipsoidal particle with semiaxes R and L covered by the shell of thickness R_0, with accumulated defects. Separation between the screening charge and the spontaneous and abrupt polarization at the core-shell interface is R_S. Ferroelectric polarization is directed along the longest ellipsoid axes.

from Huang *et al.* [15] and exactly following their derivation in the paper, the deformation η leads to the changes of the spherical particle radius for the value $\delta R = \eta R_0$ and thus to the appearance or tangential and normal stresses $\sigma_{tt} = Y\frac{\delta R}{R}$ and $\sigma_{rr} = -Y\frac{\delta R}{R}\frac{R_0}{R}$, correspondingly, where Y is the Young modulus. To adjust our results with notations used in Ref. [15], note that $R = Na$, $\delta R = n\delta a$, and so $n/N \approx R_0/R$. Finally, using $Y = 1/(s_{11} + s_{12})$ and for cubic symmetry, while it should be substituted by the factor for a wire $Y \to 1/(s_{11} + 2s_{12})$ [17], the hydrostatic pressure acting on the inner part of the ellipsoidal particle with semiaxes R and L acquires the form

$$\sigma_{rr}(R,x) = \begin{cases} \frac{-\eta(x)}{s_{11}(x)+s_{12}(x)}\frac{R_0^2(x)}{R^2}, & R \ll L \ \text{(prolate ellipsoid)}, \\ \frac{-\eta(x)}{s_{11}(x)+2s_{12}(x)}\frac{R_0^2(x)}{R^2}, & R \approx L \ \text{(sphere)}. \end{cases} \tag{1}$$

Here, subscript rr denotes that the pressure is radial, and R is the particle radius. $s_{ij}(x)$ is the elastic compliance modulus of the material, and the characteristic size $R_0(x)$ is the particle surface layer thickness, where accumulated defects create elementary volume changes. Parameter $\eta(x)$ is a "compositional" Vegard strain [36–38] that is usually dependent on the Nb content x in $KTa_{1-x}Nb_xO_3$ due to the strong dependence of the elementary volume changes on defect and surrounding atoms type [38]. Immediately, the Vegard strain x dependence can lead to the analogous dependence of the shell thickness $R_0(x)$. Moreover, the following correlation should exist: the higher the Vegard strain, the thicker the shell, because more numbers of layers are required for the full relaxation of the surface strain. Note that the stress σ_{rr} in Eq. (1) is radius (R) and content (x) dependent; and its x dependence can be determined from our experimental data. With increasing R, the stress decreases proportionally to the ratio (R_0^2/R^2).

2. *Model for depolarization field calculations in ferroelectric nanoparticles covered with a paraelectric shell*

In accordance with the Poisson equation $divD = \rho_{\text{free}}$, an internal electric field is inevitably present in a nanoparticle with inhomogeneous polarization **P** that creates nonzero divergence inside the particle, $div\mathbf{P} \neq 0$, as well as when the polarization normal component is abrupt at the particle surface [17–20], and the field is depolarizing. The field is exactly zero only for the case of the ferroelectric nanowire with polarization directed along its axis [17]; it can be regarded negligibly small for ellipsoidal particles with semiaxes R and L and polarization directed along the long axes L, if the aspect ratio R/L is very high (more than 10^3).

Since we postulated the shell layer enriched by defects, the strong polarization gradient is very likely here. First, let us estimate the "maximal" depolarization field created by an ellipsoidal single-domain ferroelectric nanoparticle core with uniform polarization $\vec{P} = (0,0,P_3)$ directed along its longer axes L, relative dielectric permittivity $\varepsilon_{33}^{\text{core}}$, and without free carriers. The core is covered by a nonferroelectric paraelectric shell with relative dielectric permittivity $\varepsilon_{33}^{\text{shell}}$, and in addition, the strong inequality $\varepsilon_{33}^{\text{shell}} \gg \varepsilon_{33}^{\text{core}}$ is likely when the shell is regarded to be in a paraelectric phase close to the ferroelectric transition. The screening charge is located either immediately outside the shell or near its outer surface, so the "effective" separation between the screening charge and the spontaneous and abrupt polarization at the core-shell interface is R_S and $R_S \leqslant R_0$. Using the inequalities $R_0 \ll R < L$, the local situation is similar to the planar ferroelectric capacitor of thickness L with a dielectric gap of thickness R_S and a depolarization field $E_3^d = \frac{-R_S P_3}{\varepsilon_0\left(R_S\,\varepsilon_{33}^{\text{core}} + L\,\varepsilon_{33}^{\text{shell}}\right)}$ [28], where ε_0 is a universal dielectric constant. It is shown that the electrostatic problem in Fig. 2 can be solved exactly for a spherical particle, i.e., $E_3^d = \frac{-(R^3-(R-R_S)^3)P_3}{\varepsilon_0((R-R_S)^3(\varepsilon_{33}^{\text{shell}}-\varepsilon_{33}^{\text{core}})+R^3(2\varepsilon_{33}^{\text{shell}}+\varepsilon_{33}^{\text{core}}))}$ where $R = L$. Using the expression and interpolation for ellipsoid depolarization field factors [47] proposed in Ref. [17], $n_D(a) \sim a^2/(1+a^2)$, where $a = R/L$, we obtain the upper estimation for the depolarization field of the ferroelectric ellipsoid covered with the paraelectric shell

$$E_3^d \approx \begin{cases} \frac{-R_S R P_3}{\varepsilon_0 \varepsilon_{33}^{\text{shell}} L^2}, & R \ll L \ \text{(very prolate ellipsoid)}, \\ \frac{-2R_S P_3}{3\varepsilon_0 \varepsilon_{33}^{\text{shell}} R}, & R \approx L \ \text{(sphere)}. \end{cases} \tag{2}$$

In reality, expression (2) gives the upper estimation of the depolarization field. In particular, if the shell is semiconducting, the value R_S acquires the sense of the Thomas-Fermi screening radius that can be much smaller than the lattice constant [48]. Also, the difference of core and shell averaged polarizations should be included in Eq. (2), i.e., one can substitute $P_3 \to (P_3 - \overline{P_3^{\text{shell}}})$.

3. *Landau-Ginsburg-Devonshire—phenomenological description*

Since the actual particle sizes for which we have experimental data are higher than 10 nm [Fig. 3(e)], in the following, we can ignore intrinsic size effects that originated from the polarization gradient, so the Landau-Ginsburg-Devonshire (LGD)-potential functional for the solid solution of paraelectric and ferroelectric acquires the relatively simple form [17–21]]:

$$\Phi = \alpha_{\text{bulk}}(T,x)\frac{P_3^2}{2} + \beta(x)\frac{P_3^4}{4} + \gamma(x)\frac{P_3^6}{6} - P_3\frac{E_3^d}{2} - Q_{ij33}\sigma_{ij}P_3^2 - \frac{1}{2}s_{ijkl}\sigma_{ij}\sigma_{kl}. \tag{3}$$

Here, x is the content of Nb in $KTa_{1-x}Nb_xO_3$. P_3 stands for the uniform polarization, E_3^d is depolarization field, and Q_{ijkl} are electrostriction tensor coefficients. As one can see from Eq. (3), the coefficient $\alpha_{\text{bulk}}(T,x)$ becomes renormalized by the stress given by Eq. (1) via the electrostriction effect [17–21], namely, $\alpha(T,R,x) = \alpha_{\text{bulk}}(T,x) - Q_{ij33}(x)\,\sigma_{ij}(R,x)$. The coefficient $\alpha(T,R,x)$ depends on temperature T, particle size R, content x, polarization orientation, and other material parameters. For ellipsoidal particles with semiaxes R and L, with polarization uniformly aligned along the longer ellipsoid axis L, the coefficient $\alpha(T,R,x)$ was calculated as

$$\alpha = \begin{cases} x\alpha_{Tf}\left(T - T_C^b\right) + (1-x)\alpha_{Tq}\left(\frac{T_q}{2}\coth\left(\frac{T_q}{2T}\right) - T_0\right) + \frac{R_S R}{\varepsilon_0\varepsilon_{33}^{\text{shell}}L^2} + \frac{4\eta(x)Q_{12}(x)}{s_{11}(x)+s_{12}(x)}\frac{R_0^2}{R^2}, & R \ll L, \\ x\alpha_{Tf}\left(T - T_C^b\right) + (1-x)\alpha_{Tq}\left(\frac{T_q}{2}\coth\left(\frac{T_q}{2T}\right) - T_0\right) + \frac{2R_S}{3\varepsilon_0\varepsilon_{33}^{\text{shell}}R} + \frac{2\eta(x)(Q_{11}(x)+2Q_{12}(x))}{s_{11}(x)+2s_{12}(x)}\frac{R_0^2}{R^2}, & R \approx L. \end{cases} \tag{4}$$

Hereinafter, subscripts q and f denote the values related to proper ferroelectrics and quantum paraelectrics, respectively. Note that the $KTa_{1-x}Nb_xO_3$ parent phase has cubic $m3m$ symmetry. Here, T_C^b is the ferroelectric Curie temperature of the bulk material. In Eq. (4), we used the Barrett-type formula for the coefficient $\alpha_q(T,R) = \alpha_{Tq}((T_q/2)\coth(T_q/2T) - T_0)$, which is valid for quantum paraelectrics [49] in a wide temperature interval, including low quantum temperatures. T_0 and T_q are the extrapolated "virtual" Curie temperature and characteristic quantum oscillations temperature, respectively. At temperatures $T \gg T_q/2$, the Barrett formulae transform into the classical limit, $\alpha_q(T,R) \approx \alpha_{Tq}(T - T_0)$. Electrostriction tensor coefficients Q_{ij} content x dependence can be regarded as linear $Q_{ij}(x) = xQ_{ij}^f + (1-x)Q_{ij}^q$. Linear dependences can also be used for elastic compliances $s_{ij}(x) = xs_{ij}^f + (1-x)s_{ij}^q$, Vegard strain $\eta(x) = x\eta_f + (1-x)\eta_q$, and shell thickness $R_0(x) = xR_f + (1-x)R_q$.

The Curie temperature $T_C(x,R)$ of the solid solution can be determined from the condition $\alpha(T_C,R,x) = 0$ that in the classical limit, $T_C \gg T_q/2$, Rgives evident analytical expressions

$$T_C(R,x) = \begin{cases} \frac{x\alpha_{Tf}T_C^b + (1-x)\alpha_{Tq}T_0 - R_S R/(\varepsilon_0\varepsilon_{33}^{\text{shell}}L^2)}{x\alpha_{Tf} + (1-x)\alpha_{Tq}} - \frac{4\eta Q_{12}(R_0^2/R^2)}{(s_{11}+s_{12})(x\alpha_{Tf}+(1-x)\alpha_{Tq})}, & R \ll L, \\ \frac{x\alpha_{Tf}T_C^b + (1-x)\alpha_{Tq}T_0 - 2R_S/(3\varepsilon_0\varepsilon_{33}^{\text{shell}}R)}{x\alpha_{Tf} + (1-x)\alpha_{Tq}} - \frac{2\eta(Q_{11}+2Q_{12})(R_0^2/R^2)}{(s_{11}+2s_{12})(x\alpha_{Tf}+(1-x)\alpha_{Tq})}, & R \approx L. \end{cases} \tag{5}$$

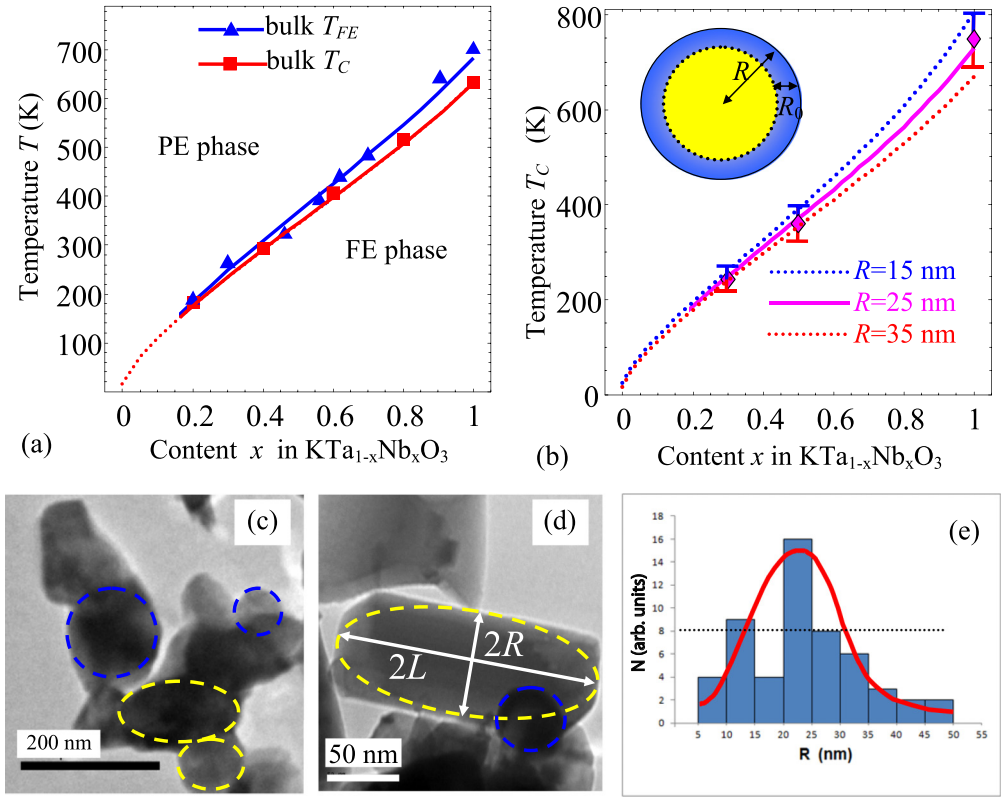

FIG. 3. (Color online) (a) Curie and ferroelectric transition temperature vs Nb content x in bulk $KTa_{1-x}Nb_xO_3$. Symbols are experimental data from Ref. [46], and solid curves are the theoretical fitting based on Eqs. (1)-(5). Abbreviations PE and FE stand for paraelectric and ferroelectric phases. Parameters of the bulk $KTaO_3$ and $KNbO_3$ are listed in Table II. (b) Curie temperature vs Nb content x in assemblies of $KTa_{1-x}Nb_xO_3$ nanoparticles. Different symbols (diamonds and bars) are experimental data, solid and dotted curves are theoretical fittings for nanoparticles with radii of 25, 15, and 35 nm, respectively. Fitting parameters are listed in Table III. (c) and (d) TEM images that show the quasispherical and ellipsoidal $KTa_{1-x}Nb_xO_3$ nanoparticles. (e) The size distribution of nanoparticles. Solid red curve is the histogram fitting by polynomial-Gaussian fit.

For the case of the second-order phase transitions, $T_C(x,R)$ is the transition temperature from the ferroelectric to paraelectric phase. For the first-order phase transitions, the condition $\alpha(T_C,R,x)=0$ still gives the Curie temperature, but the ferroelectric-paraelectric transition temperature $T_{FE}(x,R)$ should be found as a solution of the transcendental equation $\alpha(T_{FE},R,x)=3\beta(x)^2/(16\gamma(x))$. The spontaneous polarization at $E=0$ is $P_0^2=(\sqrt{\beta^2-4\alpha\gamma}-\beta)/2\gamma$.

As one can see from Eq. (5), the size-dependent shift of the Curie temperature is induced by the joint action of the depolarization field and Vegard strain, and the latter is reflected by the product $\eta(R_0/R)^2$. For the case of the negligible depolarization contribution (e.g., at $\varepsilon_{33}^{\text{shell}}\to\infty$), the radius dependence of the Curie temperature shift is governed by the ratio $(R_0/R)^2$. Equation (5) shows that the increase of the Curie temperature in comparison with a bulk material can appear under the condition $\eta(x)(Q_{11}(x)+2Q_{12}(x))<0$ for spherical particles, or $\eta(x)Q_{12}(x)<0$ for ellipsoidal particles with high aspect ratio $L/R\gg 1$.

III. Nb CONTENT AND SIZE DEPENDENCE OF THE NANOPARTICLE TRANSITION TEMPERATURE

To fit the experimental dependence of the Curie temperature $T_C(x)$ [squares in Fig. 3(a)] and ferroelectric transition temperature $T_{FE}(x)$ [triangles in Fig. 3(a)] on the content x of Nb, we use the interpolate function for $T_0(x)=T_0(1+25(1-x)^{0.7})$. Our fitting, based on Eqs. (1)–(5), is shown by solid curves for $T_{FE}(x)$ and dotted curves for $T_C(x)$. Corresponding parameters of the bulk $KTaO_3$ and $KNbO_3$ are listed in Table II.

Table II gives us the parameters of the bulk materials, but the composition dependences of the Vegard strain coefficient and shell thickness, which determine the strength of the size effects in nanoparticles in accordance with, e.g., Eq. (4), remain unknown.

To obtain the dependences, we performed the comparison with our experiment. The $KTa_{1-x}Nb_xO_3$ nanoparticle fabrication process is described in detail in Refs. [8,11,12]. Examples of transmission electron microscopy (TEM) images, which show the nanoparticles of quasispherical and ellipsoidal shape, can be seen in Figs. 3(c) and 3(d). Most of the fabricated nanoparticles have a quasispherical shape; their radii are distributed around the most probable size of 20–25 nm [see histogram in Fig. 3(e)]. The full width at half-maximum (FWHM) of the particle size distribution is about 20 nm. Although there were sizable amounts of large nanoparticles, they contributed almost nothing to the studied size effects, acting as a background and slightly elongating the error bars of the Curie temperature to lower temperatures. Experimentally,

TABLE II. Parameters of the bulk $KTaO_3$ and $KNbO_3$ extracted from Refs. [10,46,50,51].

Physical quantity	Quantum paraelectric $KTaO_3$	Ferroelectric $KNbO_3$
Coefficient α_T	$\alpha_{Tq} = 1.36 \times 10^6$m/(FK)	$\alpha_{Tf} = 4.6 \times 10^5$ m/(FK)
Characteristic temperatures	$T_q = 55$ K, $T_0 = 15$ K	$T_C = 633$ K, $T_{FE} = 698$ K
Electrostriction coefficients	$Q_{11} = 0.11$ m^4/C^2,	$Q_{11} = 0.13$ m^4/C^2,
	$Q_{12} = -0.023$ m^4/C^2	$Q_{12} = -0.047$ m^4/C^2
Elastic compliances	$s_{11} = 2.7 \times 10^{-12}$ Pa^{-1}	$s_{11} = 4.61 \times 10^{-12}$ Pa^{-1}
	$s_{12} = -6.25 \times 10^{-13}$ Pa^{-1}	$s_{12} = -1.11 \times 10^{-12}$ Pa^{-1}

the Curie temperature was determined from Raman scattering measurements using a Jobin Yvon/Horiba T64000 triple Raman spectrometer. The temperature dependences of intensity, width, and frequency of relevant modes of the Raman spectra were thoroughly analyzed. The experimental technique was described in detail in Refs. [11,12].

Comparison of the calculated Curie temperature with experimental results for $KTa_{1-x}Nb_xO_3$ nanoparticles is shown in Fig. 3(b). We attributed the diamonds in the figure to experimental data for nanoparticles with the most probable radius of 25 nm. Error bars show the Curie temperature scattering that originated from the particle radii deviation from 25 nm or about ± 10 nm that corresponds to the radii from 15 to 35 nm. Solid and dotted curves show the corresponding theoretical fitting for the 25, 15, and 35 nm radii. Note the pronounced increase of the Curie temperature for $KTa_{1-x}Nb_xO_3$ nanoparticles in comparison with a bulk solid solution for $x > 0.8$, leading to a strong enhancement of the ferroelectric properties. Since $Q_{12}(x) < 0$ and $Q_{11}(x) + 2Q_{12}(x) > 0$ for all x, the negative Vegard strain $\eta(x)$ increases the Curie temperature for spherical nanoparticles, and positive strains $\eta(x)$ increase the temperature for the prolate ellipsoids accordingly per Eq. (5).

Note that the depolarization field contribution, proportional to $R_S/(\varepsilon_0 \varepsilon_{33}^{\text{shell}} \alpha_{Tf} R)$, decreases the Curie temperature by hundreds of degrees Kelvin for a spherical nanoparticle with shell permittivity $\varepsilon_{33}^{\text{shell}}$ less than 10^3 and the thickness ratio R_S/R more than 10^{-2}, but our experiment reveals a noticeable increase of the nanoparticles' Curie temperature ($\bar{T}_C$) in comparison with a bulk one (Table III). Moreover, the depolarization field contribution can strongly dominate the Vegard one. Thus, in order to explain the experimental enhancement of $\bar{T}_C$, we should assume that the depolarization field contribution leads to a Curie temperature decrease much smaller than dozens of degrees Kelvin. This is readily possible for a semiconducting shell with $\varepsilon_{33}^{\text{shell}} \gg 10^3$ and $R_S/R < 10^{-2}$. Content-dependent parameters determined from the fitting to experiment are listed in Table III.

We found out that the best fitting of the Curie temperature for the quasispherical particles of radius (25 ± 10 nm) corresponds to the negative Vegard strain $\eta(x) = -0.01x - 0.03(1-x)$ and shell thickness $R_0(x) = (2.4x + 4.2(1-x))$ nm. The latter values are quite reasonable and correspond to the 6- to 10-unit-cell-thick shell. As anticipated, effective sphere fractions in the composite appeared rather high, $g(x) = 0.95x + 0.9(1-x)$, but some small amount of prolate ellipsoidal particles (from 5% to 10%, depending on the content x) exists due to the presence of elongated particles with high aspect ratio $L/R \gg 1$.

Here, an important remark should be made. We failed to fit the experimental data using both effective surface tension and intrinsic size effect models [17,18] for the realistic values of the surface stress coefficient; such a fitting required very high negative values of the coefficient (about $-(10-20)$ N/m), which is in contradiction to the surface equilibrium and realistic range of the coefficient $+(1$–$2)$ N/m in different perovskites and other oxides [22]. Inclusion of the intrinsic size effect (polarization gradient along with induced depolarization field) leads to the correct trend that agrees with the experiment, namely, to the Curie temperature increase with radius decrease, only at negative extrapolation lengths, and the increase becomes noticeable at a particle radius of less than 5 nm. Since there is no solid background for the existence of the negative extrapolation length and the minimal particle radius represented in the histogram is

TABLE III. Parameters of the nanosized $KTa_{1-x}Nb_xO_3$[a].

Experimental data for Curie temperature in $KTa_{1-x}Nb_xO_3$		Content-dependent parameters determined from the fitting to experiment shown in Fig. 3(b)		
Content x	Curie temperature $T_C = \bar{T}_C \pm \Delta T$	Sphere fraction $g(x) = xg_f + (1-x)g_q$ $g_f = 0.95$, $g_q = 0.9$	Shell thickness $R_0(x) = xR_f + (1-x)R_q$ $R_f = 4.2$ nm, $R_q = 2.4$ nm	Vegard coefficient $\eta(x) = x\eta_f + (1-x)\eta_q$ $\eta_f = -3\%$, $\eta_q = -1\%$
$x = 0.3$	$T_C = (243 \pm 30)$ K bulk $T_C = 238$ K	0.915	2.8 nm	-1.6%
$x = 0.5$	$T_C = (359 \pm 40)$ K bulk $T_C = 351$ K	0.925	3.3 nm	-2%
$x = 1$	$T_C = (748 \pm 50)$ K bulk $T_C = 633$ K	0.95	4.2 nm	-3%

[a]To switch off the depolarization contribution, the shell permittivity $\varepsilon_{33}^{\text{shell}}$ was chosen more than 10^4 and R_S less than 0.5 nm.

5 nm [Fig. 3(e)], inclusion of the intrinsic size effect does not help us describe the experiment. In contrast, the model based on the Vegard strain appeared in quantitative agreement with the experimental results for realistic values of all fitting parameters. The surface bond contraction model [15] gives the same radius dependence of the Curie temperature shift as that of the Vegard strain-based model, but it does not allow quantitative fitting of the experimental data dependence on Nb content x, since only the Young modulus Y is x dependent in the factor $\chi = \frac{4Y}{\alpha_T}\frac{\delta a}{a}(na)^2$ included in the model (see Table I). Substitution of the known dependence $Y(x)$ does not lead to a reasonable fitting. Other factors, such as the surface bond contraction and the lattice parameter, are almost content independent. The surface bond contraction model is probably adequate for the nanoparticles without surface defects.

Since we extract the dependence of the Vegard strain and shell thickness on Nb content x from experimental data in an unambiguous way, we can reliably enough reconstruct the impact of size effects on the nanosized $KTa_{1-x}Nb_xO_3$ using these dependences and vary the particle radius and the sphere-to-ellipsoid ratio in the particle assembly, because these factors can be controlled in realistic experiments. Such a procedure allows the opportunity to predict the Vegard strain impact on the extrinsic size effects in nanoparticles. Thus, let us consider a $KTa_{1-x}Nb_xO_3$ nanocomposite, where particle sizes are distributed around the average value, and the particle shape varies, namely, there are some fraction of ellipsoidal and spherical particles in the material, but electric and elastic interaction between the particles can be regarded as small due to the screening effects and surface stresses in the interfacial regions. Using Eqs. (1)–(5) and the parameters listed in Tables II and III, we study content and radius dependences of the extrinsic size effects in the composites with the fraction of spheres varying from 100% to 0%. Reconstructed dependences of the Curie temperature on Nb content x and particle radius R are depicted in Figs. 4 and 5.

Curie temperature increases with the increase of Nb content in bulk $KTa_{1-x}Nb_xO_3$ (dotted curves in Fig. 4). Unexpectedly, the Curie temperature $T_C(x,R)$ nonmonotonically depends on Nb content x in assemblies of small ($R = 15$ nm) $KTa_{1-x}Nb_xO_3$ nanoparticles, when the fraction of spheres becomes less than 50% for the negative Vegard strain $\eta(x) = -0.01x - 0.03(1-x)$ [Fig. 4(a)]. Such unexpected behavior could not be described as the consequence of particle shape changes, since the latter was constant under the increase of x. At the same time, the change of composition leads to the changes of the terms $\frac{4\eta(x)Q_{12}(x)}{s_{11}(x)+s_{12}(x)}\frac{R_0^2(x)}{R^2}$ and $\frac{2\eta(x)(Q_{11}(x)+2Q_{12}(x))}{s_{11}(x)+2s_{12}(x)}\frac{R_0^2(x)}{R^2}$ in Eqs. (4) and (5), proportional to the Vegard strain $\eta(x)$, which changes in a strong way with composition x, according to Table III. Thus, the nonmonotonic behavior is a direct sequence of the rather strong increase of the Vegard strain with increasing x. When the fraction of spheres is higher than 50%, the Curie temperature monotonically and superlinearly increases with an x increase and can overcome the bulk Curie temperature by hundreds of degrees Kelvin for $x > 0.8$.

Figure 4(b) illustrates how the Curie temperature changes for the positive Vegard strain $\eta(x) = 0.01x + 0.03(1-x)$ and the same parameters as in Fig. 4(a). Qualitatively, the

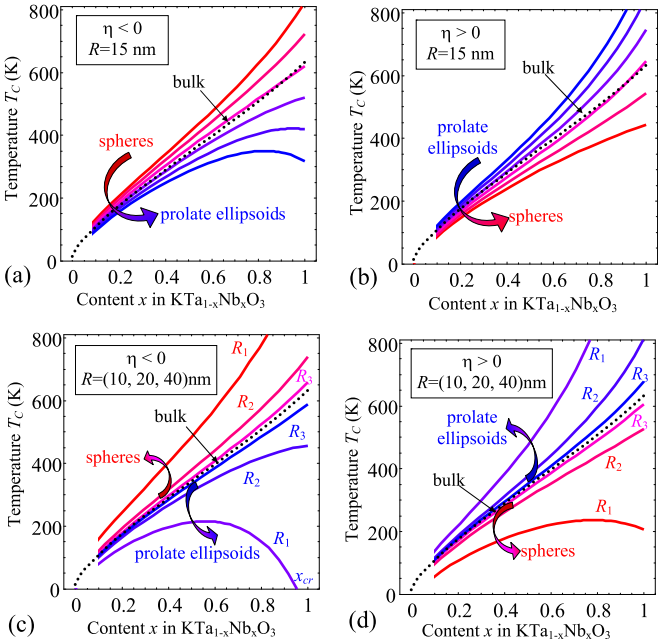

FIG. 4. (Color online) Curie temperature vs Nb content x in nanosized $KTa_{1-x}Nb_xO_3$. Plots are calculated for negative (a) and (c) and positive (b) and (d) Vegard strains. The particle radius is 15 nm in plots (a) and (b). The sphere fraction changes from 100% to 0%, with a step of 20% for different curves in the direction indicated by arrows. Plots (c) and (d) are calculated for different particle shapes (prolate ellipsoids and spheres as indicated by arrows) and radii 10, 20, and 40 nm (indicated by labels R_i near the curves). Material parameters are listed in Tables II and III.

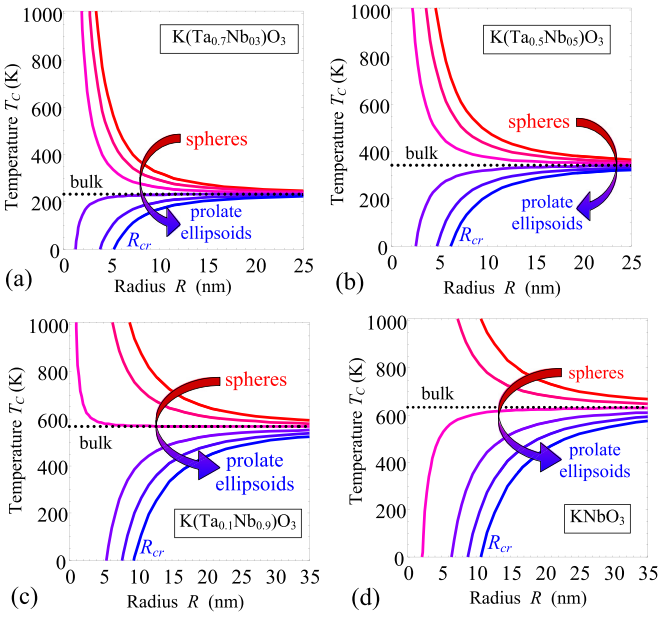

FIG. 5. (Color online) Curie temperature vs particle radii R, calculated for Vegard strain at Nb content $x = 0.3$ (a), $x = 0.5$ (b), $x = 0.9$ (c), and $x = 1$ (d). The spheres fraction changes from 100% to 0%, with a step of 20% for different curves in the direction indicated by arrows. Material parameters are listed in Tables II and III.

behavior for positive $\eta(x)$ is complementary to the one for negative $\eta(x)$ [compare Figs. 4(a) and 4(b)]. Namely, for $\eta(x) > 0$ sublinear x dependence of T_C appears when the fraction of prolate ellipsoids becomes less than 50%. The Curie temperature monotonically and superlinearly increases with the Nb content increase and can overcome the bulk Curie temperature when the fraction of spheres is lower than 50%.

These results support the statement that the principal behavior of the Curie temperature is governed by the Vegard strain sign (compression or tension), its absolute value, and particle shape (prolate or spherical one). In particular, one can see from Figs. 4(a) and 4(b), which correspond to the opposite signs of the Vegard strain, that for positive η values, the curves for prolate ellipsoidal nanoparticles are located above the dotted curve corresponding to the bulk material; curves for spherical nanoparticles are located below the dotted curve. The curve sequence is the opposite for negative η values. The curve order and slope change with respect to the bulk dotted curve, with the changing fraction of spheres. In numbers, the transition temperature in the nanosized composite could be from tens to hundreds of degrees Kelvin lower or higher than in the bulk $KTa_{1-x}Nb_xO_3$.

The smaller the particle radius R *is*, the stronger the deviation of the curves from the dotted bulk ones [Fig. 4(c)] is. Size effects are visible for the radii of less than 50 nm, and the minimal content of Nb required for the ferroelectricity appearance is different for bulk material (20%) and nanoparticles (from 10% to 30%), depending on the particle size, shape, and Vegard strain sign. In the case of the negative Vegard strain ($\eta(x) < 0$), the ellipsoids are characterized by the nonmonotonic dependence of the Curie temperature on the Nb content x, having a maximum at $x = 0.6$ and the second critical concentration of Nb, $x = 0.95$, at which ferroelectric order disappears. Figure 4(d) illustrates a model situation, when $\eta(x) > 0$ and other parameters are the same as for Fig. 4(c). One could see from this figure that it is possible to have a nonmonotonic dependence of the Curie temperature on Nb content for spherical nanoparticles of small radius; for the prolate ellipsoids, the Curie temperature monotonically increases with the increase of Nb content with the superlinear trend.

Reconstructed dependences of the Curie temperature via particle radius are shown in Fig. 5 for different x and sphere-to-ellipsoid ratios. At fixed content x, the Curie temperature T_C tends to the bulk value with the particle radius increase. With the radius decrease, we see either the strong increase of T_C proportional to R_0^2/R^2 for the negative product $\eta(2Q_{12} + Q_{11})$ or ηQ_{12} for spherical or prolate nanoparticles, respectively [see Eq. (5)], or its rapid decrease up to $T = 0$ K at some "critical" radius R_{cr} in the opposite case (compare top and bottom curves in Fig. 5). The critical radius R_{cr} of the ferroelectricity disappearance exists for the positive product $\eta(2Q_{12} + Q_{11})$ or ηQ_{12} for spherical or prolate nanoparticles, respectively. R_{cr} increases with the increase of the η absolute value.

The strong changes in the radius dependence of the Curie temperature T_C appeared when the fraction of spheres varies from 100% to 0%. Actually, in the composite with compressed spherical nanoparticles ($\eta < 0$), T_C increases with the radius decrease. Increasing the fraction of prolate ellipsoids, T_C gradually decreases, becomes lower than the bulk one, and rapidly decreases with the radius decrease in the composite with 50%, 20%, and 0% of spheres. Note, that the situation is vice versa for particles under tensile strains, $\eta > 0$; here the temperature increases as the fraction of prolate particles increases.

IV. SUMMARY

We proposed a phenomenological description of size effects in ferroelectric nanoparticles taking into account Vegard strains caused by defect accumulation near the surface of the particle. Performing calculations and detailed quantitative comparison with experimental results on quasispherical $KTa_{1-x}Nb_xO_3$ nanoparticles (average radius 25 nm) allowed us to determine the key impact of the Vegard strain on the extrinsic size effects and reveal the essential (about 100 K) increase of the transition temperature in nanoparticles compared with bulk crystals.

We also determined the dependence of the Vegard strains on the Nb content, and using this dependence, we reconstructed the content dependence of the solid solution Curie temperature. The dependence of the Curie temperature on the Nb content should be nonmonotonic for the small elongated $KTa_{1-x}Nb_xO_3$ nanoparticles (at size <30 nm).

In this way, it is established that the key role in the origin of extrinsic size effects in nanoparticles belongs to the accumulation of intrinsic and extrinsic defects near the surface that cause local Vegard strains. The strains can govern the main features of the particles' ferroelectric properties.

[1] D. Yadlovker and S. Berger, Phys. Rev. B **71**, 184112 (2005).

[2] D. Yadlovker and S. Berger, Appl. Phys. Lett. **91**, 173104 (2007).

[3] D. Yadlovker and S. Berger, J. Appl. Phys. **101**, 034304 (2007).

[4] M. H. Frey and D. A. Payne, Phys. Rev. B **54**, 3158 (1996).

[5] Z. Zhao, V. Buscaglia, M. Viviani, M. T. Buscaglia, L. Mitoseriu, A. Testino, M. Nygren, M. Johnsson, and P. Nanni, Phys. Rev. B **70**, 024107 (2004).

[6] E. Erdem, H.-C. Semmelhack, R. Bottcher, H. Rumpf, J. Banys, A. Matthes, H.-J. Glasel, D. Hirsch, and E. Hartmann, J. Phys.: Condens. Matter. **18**, 3861 (2006).

[7] I. S. Golovina, S. P. Kolesnik, I. N. Geifman, and A. A. Andriiko, Ferroelectrics **416**, 133 (2011).

[8] I. S. Golovina, S. P. Kolesnik, V. Bryksa, V. V. Strelchuk, I. B. Yanchuk, I. N. Geifman, S. A. Khainakov, S. V. Svechnikov, and A. N. Morozovska, Physica B **407**, 614 (2012).

[9] I. S. Golovina, B. D. Shanina, S. P. Kolesnik, I. N. Geifman, and A. A. Andriiko, Phys. Status Solidi B **249**, 2263 (2012).

[10] I. S. Golovina, I. N. Geifman, and M. Prokopiv, Ukr. Phys. J. **57**, 63 (2012).

[11] I. S. Golovina, V. P. Bryksa, V. V. Strelchuk, I. N. Geifman, and A. A. Andriiko, J. Appl. Phys. **113**, 144103 (2013).

[12] I. S. Golovina, V. P. Bryksa, V. V. Strelchuk, and I. N. Geifman, Functional Materials **20**, 75 (2013).
[13] I. S. Golovina, B. D. Shanina, S. P. Kolesnik, I. N. Geifman, and A. A. Andriiko, J. Appl. Phys. **114**, 174106 (2013).
[14] P. Perriat, J. C. Niepce, and G. Caboche, J. Therm. Anal. Calorim. **41**, 635 (1994).
[15] H. Huang, C. Q Sun, and P. Hing, J. Phys.: Condens. Matter **12**, L127 (2000).
[16] H. Haitao, C. Q. Sun, Z. Tianshu, and P. Hing, Phys. Rev. B **63**, 184112 (2001).
[17] A. N. Morozovska, E. A. Eliseev, and M. D. Glinchuk, Phys. Rev. B **73**, 214106 (2006).
[18] A. N. Morozovska, M. D. Glinchuk, and E. A. Eliseev, Phys. Rev. B **76**, 014102 (2007).
[19] M. D. Glinchuk, E. A. Eliseev, A. N. Morozovska, and R. Blinc, Phys. Rev. B **77**, 024106 (2008).
[20] A. N. Morozovska, M. D. Glinchuk, Rakesh K. Behera, B. Y. Zaylichniy, Chaitanya S. Deo, and E. A. Eliseev, Phys. Rev. B **84**, 205403 (2011).
[21] E. A. Eliseev, M. D. Glinchuk, V. V. Khist, C.-W. Lee, C. S. Deo, R. K. Behera, and A. N. Morozovska, J. Appl. Phys. **113**, 024107 (2013).
[22] W. Ma. Appl. Phys. A **96**, 915 (2009).
[23] V. A. Shchukin and D. Bimberg, Rev. Mod. Phys., **71**, 1125 (1999).
[24] A. K. Tagantsev, G. Gerra, and N. Setter, Phys. Rev. B **77**, 174111 (2008).
[25] R. Kretschmer and K. Binder, Phys. Rev. B **20**, 1065 (1979).
[26] C.-L. Jia, V. Nagarajan, J.-Q. He, L. Houben, T. Zhao, R. Ramesh, K. Urban, and R. Waser, Nat. Mater. **6**. 64 (2007).
[27] E. A. Eliseev, A. N. Morozovska, M. D. Glinchuk, and R. Blinc, Phys. Rev. B **79**, 165433 (2009).
[28] A. K. Tagantsev and G. Gerra, J. Appl. Phys. **100**, 051607 (2006).
[29] F. Wang, Z. Pang, L. Lin, S. Fang, Y. Dai, and S. Han, Phys. Rev. B **80**, 144424 (2009).
[30] J. Carrasco, F. Illas, N. Lopez, E. A. Kotomin, Yu. F. Zhukovskii, R. A. Evarestov, Yu. A. Mastrikov, S. Piskunov, and J. Maier, Phys. Rev. B **73**, 064106 (2006).
[31] H. Jin, Y. Dai, BaiBiao Huang, and M.-H. Whangbo, Appl. Phys. Lett. **94**, 162505 (2009).
[32] K. R. Brown, and D. A. Bonnell, J. Am. Ceram. Soc. **82**, 2431 (1999).
[33] Y. Xiao, V. B. Shenoy, and K. Bhattacharya, Phys. Rev. Lett. **95**, 247603 (2005).
[34] B. W. Sheldon and V. B. Shenoy, Phys. Rev. Lett. **106**, 216104 (2011).
[35] G. B. Stephenson and M. J. Highland, Phys. Rev. B **84**, 064107 (2011).
[36] G. Catalan and James F. Scott, Adv. Mater. **21**, 2463 (2009).
[37] X. Zhang, A. M. Sastry, and W. Shyy, J. Electrochem. Soc. **155**, A542 (2008).
[38] D. A. Freedman, D. Roundy, and T. A. Arias, Phys. Rev. B **80**, 064108 (2009).
[39] T. Ohnishi, K. Shibuya, T. Yamamoto, and M. Lippmaa, J. Appl. Phys. **103**, 103703 (2008).
[40] C. M. Brooks, L. F. Kourkoutis, T. Heeg, J. Schubert, D. A. Muller, and D. G. Schlom, Appl. Phys. Lett. **94**, 162905 (2009).
[41] P. S. Sankara, R. Krishnan, A. N. Morozovska, E. A. Eliseev, Q. M. Ramasse, D.Kepaptsoglou, W.-I. Liang, Y.-H. Chu, P. Munroe, and V. Nagarajan, J. Appl. Phys. **115**, 054103 (2014).
[42] A. N. Morozovska, E. A. Eliseev, P. S. Sankara Rama Krishnan, A. Tselev, E. Strelkov, A. Borisevich, O. V. Varenyk, N. V. Morozovsky, P. Munroe, S. V. Kalinin, and V. Nagarajan, Phys. Rev. B **89**, 054102 (2014).
[43] M. S. Kilic, M. Z. Bazant, and A. Ajdari, Phys. Rev. E **75**, 021502 (2007).
[44] M. S. Kilic, M. Z. Bazant, and A. Ajdari, Phys. Rev. E **75**, 021503 (2007).
[45] M. E. Lines and A. M. Glass, *Principles and Application of Ferroelectrics and Related Materials* (Clarendon Press, Oxford, 1977).
[46] S. Triebwasser, Phys. Rev. **114**, 63 (1959).
[47] L. D. Landau and E. M. Lifshitz, *Electrodynamics of Continuous Media* (Butterworth Heinemann, Oxford, 1980).
[48] J. Wang, A. K. Tagantsev, and N. Setter, Phys. Rev. B **83**, 014104 (2011).
[49] J. H. Barrett, Phys. Rev. **86**, 118 (1952).
[50] H. Uwe and T. Sakudo, J. Phys. Soc. Jpn. **38**, 183 (1975).
[51] L. Liang, Y. L. Li, L.-Q. Chen, S. Y. Hu, and G.-H. Lu, J. Appl. Phys. **106**, 104118 (2009).